



## 저작자표시-비영리-변경금지 2.0 대한민국

이용자는 아래의 조건을 따르는 경우에 한하여 자유롭게

- 이 저작물을 복제, 배포, 전송, 전시, 공연 및 방송할 수 있습니다.

다음과 같은 조건을 따라야 합니다:



저작자표시. 귀하는 원저작자를 표시하여야 합니다.



비영리. 귀하는 이 저작물을 영리 목적으로 이용할 수 없습니다.



변경금지. 귀하는 이 저작물을 개작, 변형 또는 가공할 수 없습니다.

- 귀하는, 이 저작물의 재이용이나 배포의 경우, 이 저작물에 적용된 이용허락조건을 명확하게 나타내어야 합니다.
- 저작권자로부터 별도의 허가를 받으면 이러한 조건들은 적용되지 않습니다.

저작권법에 따른 이용자의 권리는 위의 내용에 의하여 영향을 받지 않습니다.

이것은 [이용허락규약\(Legal Code\)](#)을 이해하기 쉽게 요약한 것입니다.

[Disclaimer](#)

공학석사 학위논문

**Multi-functional interface for high-  
rate and long-durable garnet-type  
solid electrolyte in lithium metal  
batteries**

리튬 메탈 전지의 고율 및 장기 내구성 가넷 형  
고체 전해질을 위한 다기능 계면 연구

2021 년 8 월

서울대학교 대학원  
재 료 공 학 부  
이 경 수

# 리튬 메탈 전지의 고율 및 장기 내구성 가넷 형 고체 전해질을 위한 다기능 계면 연구

Multi-functional interface for high-rate and long-durable  
garnet-type solid electrolyte in lithium metal batteries

지도 교수 강 기 석

이 논문을 공학석사 학위논문으로 제출함  
2021 년 8 월

서울대학교 대학원  
재료공학부  
이 경 수

이경수의 공학석사 학위论문을 인준함  
2021 년 6월

위 원 장	<u>홍성현</u>
부위원장	<u>강기석</u>
위 원	<u>최장욱</u>

# Abstract

## **Multi-functional interface for high-rate and long-durable garnet-type solid electrolyte in lithium metal batteries**

Kyeong-su Lee

Department of Material Science and Engineering

College of Engineering

The Graduate School

Seoul National University

The growth of lithium dendrite in solid electrolytes is one of the major unexpected obstacles to the commercialization of solid-state batteries based on garnet-type solid electrolytes. The poor interface with lithium metal and the non-negligible electronic conductivity of the solid electrolyte have been pointed out as the two major causes of this growth. Although various attempts have been recently made to address each issue, the employment of garnet-type solid electrolytes still suffers from a low critical current density and inferior cycle performance. Herein, we propose a novel strategy that can simultaneously resolve both the interface and electronic conductivity issues via a simple one-step procedure that provides multi-layer protection at low temperature. By taking advantage of the facile chemical conversion reaction of metal fluoride, we show that the wet coating of  $\text{SnF}_2$  particles on the solid electrolyte effectively produces a multi-functional interface composed of  $\text{LiF}$  and  $\text{Li-Sn}$  alloy upon contact with lithium. It is unraveled that it

surprisingly results in the conformal coating of the LiF layer, which significantly lowers the interfacial resistance and blocks the leakage current to the solid electrolyte. Moreover, micro-sized Li–Sn alloys formed inside the Li metal promote the prolonged interfacial stability, especially during high-current stripping, by suppressing the void formation, which is attributed to the fast lithium kinetics in the alloying medium. We demonstrate that this multi-function enables the remarkably high critical current density value up to  $2.4 \text{ mA cm}^{-2}$  at room temperature and the stable galvanostatic cycling for over 1000 hours at  $0.5 \text{ mA cm}^{-2}$  in the lithium symmetric cell. Moreover, the full cell employing the modified garnet electrolyte delivers an unprecedentedly robust cycle life of more than 600 cycles at a current density of  $1.0 \text{ mA cm}^{-2}$ , which is the highest performance achieved at room temperature reported to date.

**Keyword : Li-ion rechargeable batteries; Garnet-type Solid electrolyte; Tin fluoride; Li dendrite; Interface;**

**Student Number : 2019-28030**

# Table of Contents

<b>Abstract .....</b>	<b>i</b>
<b>List of Figures .....</b>	<b>v</b>
<b>Chapter 1. Introduction .....</b>	<b>1</b>
1.1 Motivation and outline.....	1
<b>Chapter 2. Experimental section .....</b>	<b>4</b>
2.1 Preparation of solid garnet electrolyte.....	4
2.2 Modification of interface.....	4
2.3 Material characterization.....	5
2.4 Electrochemical measurement.....	5
2.5 Full cell fabrication.....	6
<b>Chapter 3. Results and discussion .....</b>	<b>7</b>
3.1 Characterization of the interface modified by SnF <sub>2</sub> .....	7
3.2 Identify the role of each artificial layer.....	16
3.3 Electrochemical properties benefiting from artificial layer...	23
<b>Chapter 4. Conclusion.....</b>	<b>30</b>

<b>References .....</b>	<b>31</b>
<b>Abstract in Korean.....</b>	<b>36</b>

## List of Figures

**Figure 1. Chronoamperometry and electrochemical impedance spectra.** **a.** Current–time curve of Au/LLZTO/Au symmetric cell at 1 V. **b.** Nyquist plot of Au/LLZTO/Au cell measured at room temperature.

**Figure 2. Structural characterization.** XRD patterns of pristine LLZTO and acid treated LLZTO pellet.

**Figure 3. Morphological and chemical characterization of SnF<sub>2</sub>-modified interface.** **a.** Photographs of SnF<sub>2</sub>-treated LLZTO reacted with Li metal at various temperatures. **b–e.** Surface SEM images of SnF<sub>2</sub> layer reacted with Li at various temperatures. **f–g.** Sn 3*d* and F 1*s* XPS spectra of the SnF<sub>2</sub> interface for various temperatures.

**Figure 4. Morphological characterization of coating layer.** Top-view EDS mapping of SnF<sub>2</sub> layer before heating, **a.** F element and **b.** Sn element, and after heating, **c.** F element and **d.** Sn element.

**Figure 5. Cross-sectional morphology and schematic illustration of interface.** **a.** Cross-sectional SEM image of the interface between SnF<sub>2</sub>-treated LLZTO and Li metal after heating at 220 °C. **b–e.** Corresponding EDS mapping of F, Sn, O, Zr elements from (a). **f.** High-resolution cross-sectional SEM images of interface and line profile of F and Sn elements. **g.** Schematic illustration of interface design.



**Figure 6. Electrochemical stability of SnF<sub>2</sub>-modified LLZTO.** **a.** EIS spectra of Li symmetric cells at room temperature **b.** Potential profile during stripping at 0.2 mA cm<sup>-2</sup>. **c.** Critical current density measurement of Li symmetric cell at room temperature.

**Figure 7. Cross-sectional morphology.** **a.** Cross-sectional SEM image of SnF<sub>2</sub>-treated LLZTO with Li metal removed. **b.** Cross-sectional SEM image of SnF<sub>2</sub>-LLZTO with new Li attached without micro-sized Li–Sn alloy. **c.** Corresponding EDS mapping of F, Zr, Sn, and O elements from (b).

**Figure 8. Delithiation/stripping experiment.** Voltage–time curve of Li/LLZTO–Sn metal powder/Li symmetric cell at 0.2 mA cm<sup>-2</sup>.

**Figure 9. Electrochemical characterization of LLZTO with 100 nm of LiF deposited.** **a.** Nyquist plot of Li/LLZTO–LiF/Li symmetric cell at room temperature. **b.** Critical current density measurement of Li/LLZTO–LiF/Li cell.

**Figure 10. Electrochemical performance of Li symmetric cells and SEM images of cycled LLZTO.** **a.** Long-term performance of Li/SnF<sub>2</sub>-treated LLZTO/Li symmetric cell with a current density of 0.5 mA cm<sup>-2</sup> at room temperature. **b.** Comparison of galvanostatic cycling for symmetric cells of uncoated LLZTO and SnF<sub>2</sub>-treated LLZTO at 0.5 mA cm<sup>-2</sup>. Cross-sectional SEM image of **c.** uncoated LLZTO interface and **d.** SnF<sub>2</sub>-treated LLZTO interface after cycling. **e–g.** Charge/discharge curves of Li/SnF<sub>2</sub>-treated LLZTO/Li cell at 1.0 mA

$\text{cm}^{-2}$  at room temperature.

**Figure 11. Cycling performance of hybrid solid-state full cell.** **a.** Long-term performance of Li/SnF<sub>2</sub>-treated LLZTO/LiFePO<sub>4</sub> hybrid full cell with a current density of  $1.0 \text{ mA cm}^{-2}$  at room temperature. **b.** Comparison of cyclability of hybrid cells of uncoated LLZTO and SnF<sub>2</sub>-treated LLZTO at  $0.1 \text{ mA cm}^{-2}$ . **c.** Rate capability of SnF<sub>2</sub>-treated LLZTO full cell at different current densities. **d.** Voltage profile of Li/SnF<sub>2</sub>-treated LLZTO/LFP cell at different rates. **e.** Performance comparison of solid-state batteries with garnet-type solid electrolyte.

**Figure 12. Voltage profile of pristine LLZTO full cell.** 1<sup>st</sup> charge curve of Li/uncoated LLZTO/LFP hybrid full cell at  $1.0 \text{ mA cm}^{-2}$  at room temperature.

**Figure 13. Electrochemical characterization of hybrid solid-state full cell.** Cycling performance of Li/SnF<sub>2</sub>-treated LLZTO/NCM111 hybrid cell at  $0.5 \text{ mA cm}^{-2}$  at room temperature.

# Chapter 1. Introduction

## 1.1 Motivation and outline

The demands for lithium-ion batteries with higher energy density and safety have recently soared with the growing interest in electric vehicles as the next-generation transportation. All-solid-state batteries that employ a lithium-metal anode are one of the most promising candidates that can offer both desirable safety and high energy density. The lithium-metal anode delivers the highest theoretical capacity ( $3860 \text{ mAh g}^{-1}$ ) and the lowest redox potential as an ideal anode material, and the use of the non-flammable solid electrolyte is expected to mitigate the critical issues of the lithium-metal anode observed in conventional liquid electrolytes.<sup>[1, 2]</sup> It is widely known that the uncontrollable lithium growth in the liquid-based cell causes the formation of an excessive solid electrolyte interphase (SEI) layer, leading to deterioration of the energy efficiency and cycle stability and initiating the short-circuit that leads to thermal runaway, posing a high risk for battery explosion.<sup>[3, 4]</sup> In contrast, the solid electrolyte is thought to be capable of preventing lithium dendrite formation owing to its high mechanical and chemical robustness. Over the past decades, progress toward the realization of solid-state lithium batteries has thus extensively been made by developing various types of solid electrolytes including sulfide-, garnet-, NASICON-, and perovskite-type materials.<sup>[5-11]</sup> Among them, the cubic garnet-type  $\text{Li}_7\text{La}_3\text{Zr}_2\text{O}_{12}$  (LLZO) is considered an attractive option owing to its interfacial stability with lithium metal, wide electrochemical window, and high ion conductivity (close to  $1 \text{ mS cm}^{-1}$  at

room temperature).<sup>[12-14]</sup> Moreover, LLZO can be easily synthesized in ambient air and is chemically stable, which is advantageous for the large-scale fabrication of solid-state batteries.<sup>[15, 16]</sup>

Recent investigations, however, have shown that a short-circuit can easily occur even in solid-state batteries, which was unexpectedly caused by lithium dendritic growth and propagation through the solid electrolyte.<sup>[17-20]</sup> Extensive research efforts have revealed that various factors may affect the abnormal lithium growth in solid-state batteries based on garnet-type electrolytes.<sup>[21, 22]</sup> In particular, the poor physical/chemical contact between the solid electrolyte and lithium was shown to be one of the major roots, causing a locally high interfacial resistance. This poor contact subsequently results in inhomogeneous lithium-ion flux through the interface, triggering preferred lithium growth/propagation at local regions such as defects and cracks. Previous attempts have thus been focused on tailoring the interfacial resistance by removing the contamination layer or introducing a lithiophilic buffer layer that enhances the wettability with lithium (*e.g.*, LiF, Al<sub>2</sub>O<sub>3</sub>, Li<sub>3</sub>PO<sub>4</sub>), which have led to partial success.<sup>[23-28]</sup> Nevertheless, it was found that even such a well-manufactured interface could not be sustainably maintained during repeated cycling, resulting in non-uniform lithium growth at the interface and premature cell failure. This phenomenon was attributed to the voids that are continuously formed at the interface during the repeated stripping process because of the sluggish lithium transport in the bulk lithium metal compared with the lithium stripping flux.<sup>[29, 30]</sup> Several studies have thus suggested that the use of an alloy or interlayers such as Li–Ag, Li–Mg, or Li–Au could improve the lithium transport kinetics in the electrode, thus mitigating the formation of voids at the interface.<sup>[31-33]</sup> More recently, it was revealed that the non-negligible electronic

conductivity of the solid electrolyte could also serve as the chief source of the dendrite formation.<sup>[34]</sup> Han *et al.* showed that the solid electrolyte could partly allow electron conduction, especially through the grain boundaries, where the lithium ions could be directly reduced. This high electronic conductivity accompanied the nucleation and growth of lithium metal along the grain boundaries during cycling, which eventually caused the short-circuit of the system.<sup>[35]</sup>

The various factors that cause abnormal lithium growth in solid-state batteries imply that there can be no single solution to resolve the short-circuit issues. Moreover, previously proposed approaches that use costly deposition equipment and/or high-temperature processes are not likely to be feasible for industrial-scale applications. Herein, we propose a multi-functional interlayer that can be simply and cost-effectively applied to the solid-state battery system at a relatively low temperature and that is capable of overcoming the key issues of the interface and the electronic conductivity, achieving markedly improved cycle stability at practically high current rates. We show that a simple one-step wet-coating procedure of metal fluoride ( $\text{SnF}_2$ ) can produce a multi-layer interface comprised of (i) an electronically insulating and lithiophilic LiF layer and (ii) a metallic lithium alloy (Li–Sn) with high ionic conductivity. It is elucidated that the wet coating of  $\text{SnF}_2$  particles results in the formation of a thin LiF layer upon contact with the lithium-metal anode, which conformally coats the electrolyte surface, filling up the defects/cracks, thereby leading to a low interfacial resistance and passivation of the leakage current. It is also shown that the Li–Sn alloys inside the lithium matrix promote the chemical diffusion of lithium, thus suppressing the lithium void formation at the interface even with the high-rate stripping process.<sup>[29]</sup>

<sup>31]</sup> The presence of the multi-functional layer in the garnet-type electrolyte enables a high critical current density up to  $2.4 \text{ mA cm}^{-2}$  at room temperature and stable cycling for over 1,000 hours at  $0.5 \text{ mA cm}^{-2}$ . Moreover, the full cell assembled with commercial cathodes such as  $\text{LiFePO}_4$  and  $\text{LiNi}_{1/3}\text{Co}_{1/3}\text{Mn}_{1/3}\text{O}_2$  delivers an unprecedentedly long cycle life ( $> 600$  cycles) at a high current density ( $\sim 1.0 \text{ mA cm}^{-2}$ ), which is the highest performance achieved at room temperature reported to date. We believe that our strategy will be widely applicable to various solid electrolytes owing to the facile and simple low-temperature process. In addition, it is further extendable to other conversion-based metal fluorides, whose exploration is expected to expedite the practical employment of garnet-type solid electrolytes in all-solid-state batteries.

## Chapter 2. Experimental section

### 2.1 Preparation of solid garnet electrolyte.

The  $\text{Li}_{6.4}\text{La}_3\text{Zr}_{1.4}\text{Ta}_{0.6}\text{O}_{12}$  (LLZTO) garnet electrolyte was synthesized using a solid-state reaction method.  $\text{LiOH}\cdot\text{H}_2\text{O}$  (99.99%, Sigma-Aldrich),  $\text{La}_2\text{O}_3$  (99.99%, Sigma-Aldrich),  $\text{Ta}_2\text{O}_5$  (99.99%, Sigma-Aldrich), and  $\text{ZrO}_2$  (99%, Sigma-Aldrich) were used as precursors. An additional of 20 wt.%  $\text{LiOH}\cdot\text{H}_2\text{O}$  was used to compensate for the Li loss during the sintering process. These starting materials were first ball milled (Pulverisette5, Fritsch) at 200 rpm for 10 hours with yttrium-stabilized zirconium oxide balls. The mixed powder was pressed into a pellet with a diameter of 15 mm and calcinated at 900 °C for 12 hours in an alumina crucible. After calcination, the pellet was ground and ball milled again for 10 hours to produce fine a LLZTO powder. The obtained powder was pressed into pellet with a diameter of 10 mm and sintered at 1100 °C for 10 hours with 0.2 wt.%  $\gamma\text{-Al}_2\text{O}_3$  (99.9%, Sigma-Aldrich) as the sintering agent. To obtain a clean surface for the solid electrolyte, the LLZTO pellet was polished with 600, 1000, and 2000 grit sandpaper and cleaned with hydrochloric acid for 15 minutes. The thickness of LLZTO was fixed at  $\sim 700\text{ }\mu\text{m}$ , and the density of the pellets was 90%–92%.

### 2.2 Modification of interface.

First, 30 mg of  $\text{SnF}_2$  powder (99%, Sigma-Aldrich) was completely dispersed in 1 mL of isopropanol solution using a stirrer at room temperature. Then, 15  $\mu\text{L}$  of

SnF<sub>2</sub> solution was slowly added dropwise onto the cleaned LLZTO pellet and dried at 60 °C in a vacuum oven to avoid contamination of the surface. A 300-μm layer of Li metal was carefully pressed onto the SnF<sub>2</sub>-treated LLZTO in an Ar-filled glove box, and then, the pellets were heated to different temperatures (120 °C, 180 °C, 220 °C) for 2 hours to form an artificial interlayer.

## **2.3 Material characterization.**

XRD (New D8 Advance, Bruker) was employed to characterize the crystal structure of LLZTO using Cu-K $\alpha$  radiation in the 2 $\theta$  range of 10°–70° with a step size of 0.02°. To observe the interface of the ceramic pellet at high resolution, a cross-section polisher (CP, IB-09020CP, JEOL) was used to prepare the sample. The specimen cross-sections were polished by an Ar<sup>+</sup> ion beam at an acceleration voltage of 7 kV and gun current of 120 μA for 8 hours. The polishing process was performed in an Ar atmosphere at –120 °C to prevent deformation of the highly reactive Li and solid electrolyte. The morphology and elemental distribution of prepared sample were investigated using SEM (Helios G4 HX, Thermo Fisher Scientific) and EDS (Ultim Extreme, Oxford Instruments). To characterize the chemical composition of the artificial interlayer, XPS was performed on an ESCALAB 250 XI (Thermo Fisher Scientific) with monochromatic Al-K $\alpha$  radiation (1486.6 eV). The XPS spectrometer was directly connected to the Ar glove box via a transfer chamber to prevent contact of the sample with moisture and air. The C 1s peak at 284.5 eV corresponding to C–C bonding was used as a reference for charge compensation.



## 2.4 Electrochemical measurements.

To measure the ionic conductivity and electronic conductivity of garnet-type solid electrolytes, both sides of the pellet were sputtered with gold (Au) as the lithium-ion blocking electrode. To reinforce adhesion with Au and LLZTO, the deposited pellet was heated to 120 °C in a glove box. The EIS spectrum measurements of the Au symmetric 2032-type coin cell were performed using a potentiostat (VSP-300, Bio-Logic Science Instruments) in the frequency range from 3 MHz to 0.1 Hz at room temperature. The DC polarization to measure electronic conductivity was conducted with an applied voltage of 1 V for 3000 seconds. The stripping measurement of the Li symmetric cell was performed using a potentio-galvanostat (WBCS 3000, WonATech) at a constant current of 0.2 mA cm<sup>-2</sup>. The critical current density was measured by galvanostatic cycling from 0.05 to 2.5 mA cm<sup>-2</sup> with increasing current at intervals of 0.1 mA cm<sup>-2</sup>, and the duration of each cycling step was 0.5 hours. The cycling stability of the symmetric cells was evaluated at current densities of 0.5 and 1.0 mA cm<sup>-2</sup> with a fixed plating/stripping interval of 0.5 hours.

## 2.5 Full cell fabrication.

To assemble full cells, the lithium iron phosphate (LFP) cathode was prepared with a mixture of LFP powder, super P carbon, and polyvinylidene fluoride binder in a weight ratio of 80:10:10. The slurry was coated on Al foil and dried at 60 °C under vacuum overnight. The areal mass loading of the active material was 3-3.5 mg cm<sup>-2</sup>. An ionic liquid (2 M LiFSI in Pyr13FSI) was used to improve the

interfacial contact with the cathode.

## Chapter 3. Results and discussion

### 3.1 Characterization of the interface modified by SnF<sub>2</sub>.

A tantalum (Ta)-doped Li<sub>6.4</sub>La<sub>3</sub>Zr<sub>1.4</sub>Ta<sub>0.6</sub>O<sub>12</sub> (LLZTO) pellet was prepared using the conventional solid-state reaction method and was employed in our study (see Experimental section for details on the sample preparation). The electrochemical impedance spectroscopy (EIS) spectra and chronoamperometry results in Figure 1 confirm that the ionic and electronic conductivities of the LLZTO were  $1.55 \times 10^{-4}$  S cm<sup>-1</sup> and  $1.57 \times 10^{-9}$  S cm<sup>-1</sup>, respectively, at room temperature, in agreement with previous literatures.<sup>[34-36]</sup> Before further investigation of the interface, the LLZTO pellet samples were immersed in 1 M hydrochloric acid for 15 minutes and immediately washed with ethanol to remove any surface contaminants. Upon exposure to the atmosphere, LLZTO is known to rapidly react with air or moisture to produce insulating Li<sub>2</sub>CO<sub>3</sub> and LiOH.<sup>[37]</sup> The X-ray diffraction (XRD) patterns of the treated samples indicate that the cubic garnet structure was well preserved while the contamination layer was successfully removed by the acid treatment (Figure 2).

The surface of the LLZTO pellet was coated by slowly adding isopropanol solution dispersed with SnF<sub>2</sub> powder dropwise at room temperature, followed by drying at 60 °C in a vacuum oven (see Experimental section for details). Subsequently, the lithium-metal disc was placed on the coated LLZTO pellet and was heated to 220 °C to promote the chemical conversion reaction to form lithium fluoride (LiF) and Sn. Figure 3a shows that the pristine pellet coated with the SnF<sub>2</sub>

layer (white) gradually turned black as the temperature increased, indicating that  $\text{SnF}_2$  had reacted with lithium metal.<sup>[38, 39]</sup> It was noted that not only the region of direct contact with the lithium-metal disc but also the whole region of the  $\text{SnF}_2$  layer reacted, indicating the relatively fast and homogeneous conversion reaction at 220 °C. This result is also partly attributable to the melting temperatures of Sn and  $\text{SnF}_2$  of approximately 232 °C and 213 °C, respectively, which are close to our heat-treatment temperature (220 °C). The scanning electron microscopy (SEM) images in Figure 3b–e confirm that the particulate morphologies of  $\text{SnF}_2$  on the as-coated pellet surface gradually changed to a homogeneous film upon increasing the temperature to 220 °C. According to the energy dispersive X-ray spectroscopy (EDS) results in Figure 4, the F elements were evenly distributed on the surface of the solid electrolyte after the drop casting, which was maintained regardless of the heat treatment. Interestingly, the Sn element was locally segregated at micrometer scales after the heat treatment at 220 °C, implying the formation of the micron-sized Li–Sn alloy after the conversion reaction, whose effects will be discussed further later. The chemical composition of the interlayer was carefully investigated using X-ray photoelectron spectroscopy (XPS), as shown in Figure 3f–g. The as-coated pellet displays only the characteristic peaks of Sn–F bonds arising from the  $\text{SnF}_2$  particles, as evidenced by the Sn 3*d* (486.5 and 495.0 eV) and F 1*s* (685.8 eV) spectra.<sup>[40]</sup> However, as the samples were heated at higher temperatures, a new F 1*s* XPS peak (684.5 eV) corresponding to Li–F gradually emerged at the expense of the Sn–F peak. Moreover, the characteristic Sn–metal peaks began to appear at 483.8 and 492.3 eV, indicating the progress of the conversion reaction between  $\text{SnF}_2$  and lithium metal.

The microstructure of the LLZTO pellet treated at 220 °C was investigated using

SEM/EDS cross-sectional image analysis. Cryo-milling using an  $\text{Ar}^+$ -ion beam was performed with extra care in an inert environment to reliably probe the submicron interlayer present between the highly reactive lithium metal and the solid electrolyte. Figure 5a shows that the LLZTO surface was covered with a thin conformal layer (a few hundreds of nanometers) of dark gray in the image. The EDS mapping in Figure 5b–e indicates that the thin layer was mostly F-rich in composition and passivated the entire LLZTO surface, even filling up the void space present near the surface. Considering the expected conversion reaction between  $\text{SnF}_2$  and lithium, the F-rich layer is believed to be mainly LiF. Meanwhile, it was observed that the Sn element exists in the form of micron-sized ( $\sim 10\ \mu\text{m}$ ) particles inside the lithium-metal matrix (Figure 5c), which is supposed to be the result of the Li–Sn alloy formation at near the melting temperature of Sn ( $232\ ^\circ\text{C}$ ) and is in agreement with the top-view EDS results in Figure 4. Additionally, a small amount of Sn was detected in the thin F-rich layer. High-resolution SEM images in back-scattered electron mode (Figure 5f) suggest that the F-rich layer was hundreds of nanometers thick and consisted of two or more phases, as indicated by the arrow in the image contrast. According to the elemental line profile in Figure 5f, the bright spots in the F-rich layer were observed to correspond to the Sn-containing phase, which is likely to be nano-sized Li–Sn alloy. Combining these EDS results with the XPS findings, we speculate that during the conversion reaction between lithium metal and  $\text{SnF}_2$ , a major portion of Sn has undergone the alloying reaction with the excess amount of lithium while some Li–Sn particles were trapped in the LiF layer on the interface. Figure 5g schematically illustrates the reaction process between the  $\text{SnF}_2$ -treated LLZTO and lithium metal and the consequent interface morphologies.

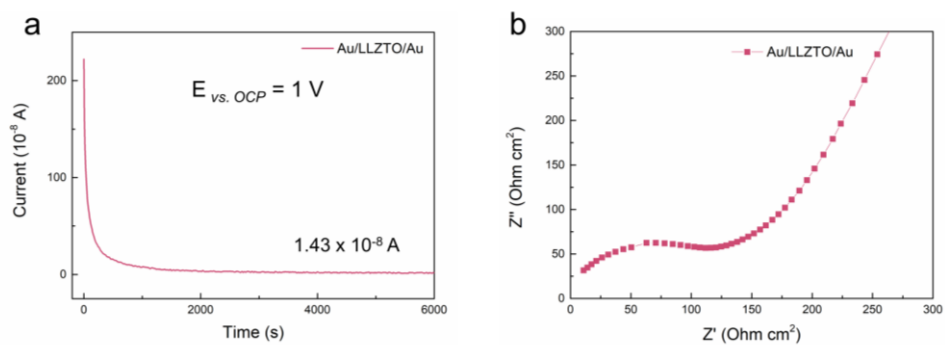


**Figure 1. Chronoamperometry and electrochemical impedance spectra. a.** Current–time curve of Au/LLZTO/Au symmetric cell at 1 V. **b.** Nyquist plot of Au/LLZTO/Au cell measured at room temperature.

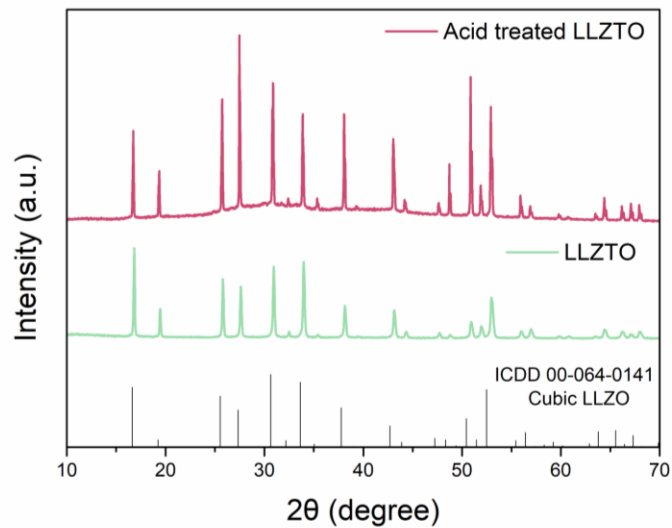


**Figure 2. Structural characterization.** XRD patterns of pristine LLZTO and acid treated LLZTO pellet.

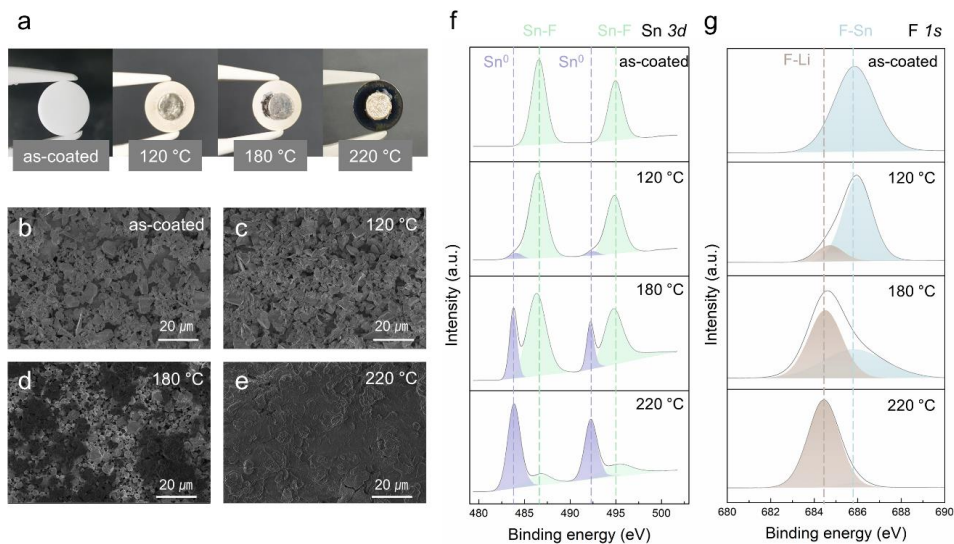


**Figure 3. Morphological and chemical characterization of SnF<sub>2</sub>-modified interface.** **a.** Photographs of SnF<sub>2</sub>-treated LLZTO reacted with Li metal at various temperatures. **b–e.** Surface SEM images of SnF<sub>2</sub> layer reacted with Li at various temperatures. **f–g.** Sn 3d and F 1s XPS spectra of the SnF<sub>2</sub> interface for various temperatures.



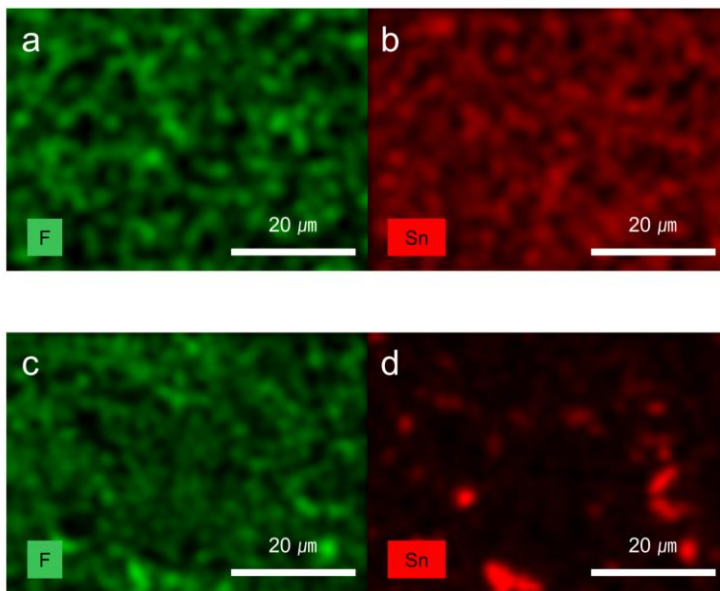


**Figure 4. Morphological characterization of coating layer.** Top-view EDS mapping of  $\text{SnF}_2$  layer before heating, **a.** F element and **b.** Sn element, and after heating, **c.** F element and **d.** Sn element.

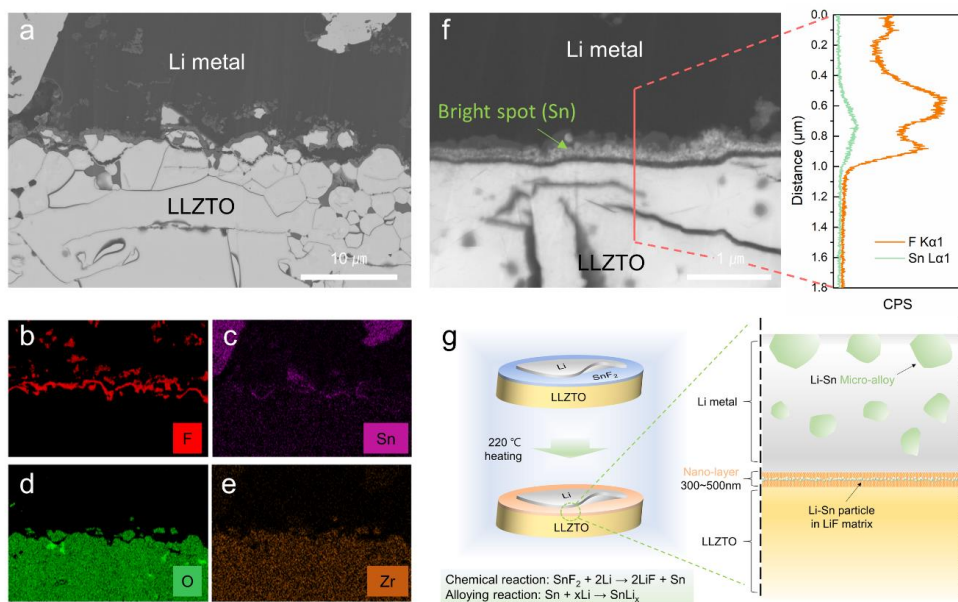


**Figure 5. Cross-sectional morphology and schematic illustration of interface. a.**

Cross-sectional SEM image of the interface between SnF<sub>2</sub>-treated LLZTO and Li metal after heating at 220  $^{\circ}\text{C}$ . **b–e.** Corresponding EDS mapping of F, Sn, O, Zr elements from (a). **f.** High-resolution cross-sectional SEM images of interface and line profile of F and Sn elements. **g.** Schematic illustration of interface design.

### 3.2 Identify the role of each artificial layer.

Investigation of the electrochemical properties of the multi-layer coated LLZTO was preliminarily conducted by measuring the EIS spectra and the critical current densities, as shown in Figure 6a–c. Li–Li symmetric cells were assembled employing SnF<sub>2</sub>-treated LLZTO as the solid electrolyte and were compared with the reference systems of the uncoated LLZTO. The electrochemical impedance spectra in Figure 6a show that the total resistance was significantly decreased from 164 to 56  $\Omega \text{ cm}^2$  by employing the SnF<sub>2</sub>-treated LLZTO as the electrolyte in the cell at room temperature. Moreover, the semicircle at low frequency that is typically attributed to the interfacial resistance became notably smaller for the SnF<sub>2</sub>-treated LLZTO compared with that of the uncoated LLZTO.<sup>[41–43]</sup> This result indicates that the interface resistance could be effectively reduced by the interlayer that was formed from the reaction between Li and SnF<sub>2</sub>. Concerning the improved interfacial property, we attempted to clarify the effect of the conformal LiF interlayer decoupled from that of the micron-sized Li–Sn alloy present in the lithium metal. In this regard, the top lithium electrode containing the alloy was physically peeled off from the LLZTO, and new fresh lithium metal was placed instead. In this process, the F-rich conformal layer was not damaged, maintaining good contact without the introduction of any voids or defects. The impedance test on the cell with the new lithium metal (hereafter, SnF<sub>2</sub>-LLZTO-New Li) indicated that the interface resistance was comparable to that of the original SnF<sub>2</sub>-treated LLZTO ( $\sim 73 \Omega \text{ cm}^2$ ), suggesting that the observed small interface resistance was mainly attributable to the conformal LiF nanolayer that could enhance the interfacial contact between lithium and the LLZTO.

We further investigated the efficacy of the multi-layer interface during the harsh lithium stripping process in the symmetric cell. Figure 6b presents the electrochemical profiles of the stripping process of the cells employing the lithium metal anode with a thickness of 300  $\mu\text{m}$  at room temperature. At a current density of 0.2  $\text{mA cm}^{-2}$ , the theoretical total depletion time (marked as  $T_0$  in the graph) was approximately 162 hours, when all the lithium was completely stripped out from the electrode. The comparison of the depletion times indicates that the  $\text{SnF}_2$ -treated LLZTO could deliver a stripping capacity close to 90% of the theoretical value (144 hours). In contrast, the symmetric cell with the uncoated LLZTO or the  $\text{SnF}_2$ -LLZTO-New Li could only deliver approximately 30% of the theoretical value ( $\sim 45$  hours), and was accompanied by the rapid growth of the overpotential after 45 hours. The significantly reduced capacity and the large overpotential during the stripping process have been previously attributed to the resistance increases at the interface, arising from the formation of the lithium voids at the interface.<sup>[1, 31]</sup> In previous literatures, it has been reported that the sluggish vacancy diffusion in the lithium metal causes the formation of voids at the interface, when the flux of lithium stripping is comparatively greater than the intrinsic vacancy diffusion rate.<sup>[29, 31]</sup> This implies that the LiF conformal layer in  $\text{SnF}_2$ -LLZTO-New Li could not contribute to mitigating the formation of the lithium voids during the stripping, but it could simply reduce the interfacial resistance, as shown in Figure 6a. The remarkable improvement of the stripping capability with the  $\text{SnF}_2$ -treated LLZTO is likely due to the presence of the Li-Sn alloy in the lithium metal, which aids in expediting the lithium transport at the interface. We suppose that the lithium-ion transport could be facilitated through the Li-Sn alloy via chemical diffusion rather than intrinsic vacancy diffusion, thereby mitigating the imbalance in the lithium

transference, resulting in high interfacial stability during the continuous stripping. Similar findings were recently reported by Krauskopf *et al.* and Meng *et al.*, who disclosed that the use of a lithium-alloy electrode could shift the lithium transport mechanism in the electrode from vacancy diffusion to more facile chemical diffusion, thereby suppressing the pore formation during stripping.<sup>[31, 44]</sup> To further support our speculation, we performed an additional experiment, where Sn metal powder (~10  $\mu\text{m}$ ) was simply placed between lithium metal and the uncoated LLZTO with the equivalent ratio/amount of the Sn used in the  $\text{SnF}_2$  coating protocols. Figure 8 demonstrates that the simple addition of the Sn metal powder could also lead to significant enhancement of the stripping capacity of the lithium metal. The result of the stripping experiment manifest that the depletion time was extended to 120 hours, similar to that of the  $\text{SnF}_2$ -treated LLZTO, even though the resistance was relatively high because of the poor interfacial contact.

The improved interfacial stability of the  $\text{SnF}_2$ -treated LLZTO, as evidenced in Figure 6a and b, could help achieve the notable increase in the critical current density (CCD) in Figure 6c. The lithium symmetric cell employing the uncoated LLZTO displayed premature short-circuit at a current rate of  $0.6 \text{ mA cm}^{-2}$ , which agrees with previous reports on typical garnet-type solid electrolytes. On the other hand, the CCD could increase to a value of  $2.4 \text{ mA cm}^{-2}$  at room temperature with the  $\text{SnF}_2$ -treated LLZTO cell. The higher CCD value suggests that the lithium dendrite formation through the solid electrolyte could be effectively suppressed even under the harsh current conditions, confirming the effectiveness of the multi-layer strategy. Meanwhile, the  $\text{SnF}_2$ -LLZTO-New Li case yielded a CCD value of  $1.8 \text{ mA cm}^{-2}$ , which suggests that the sole presence of the LiF conformal interlayer could also contribute to reducing the risk of short-circuit to some extent. These

series of electrochemical footprints suggest the multifunction of the interlayer, *i.e.*, (i) the LiF conformal layer reduces the interfacial resistance while serving as an electronic insulating buffer, and (ii) the micro-alloy aids in the lithium-transport kinetics to prevent pore formation at the interface. Nevertheless, it is noteworthy that our LiF-based interlayer on the LLZTO has a thickness of a few hundred nanometers, and considering the intrinsically low ionic conductivity of the LiF, it would cause a substantial overpotential in the cell operation.<sup>[26, 45, 46, 47]</sup> Moreover, according to our own experiments in Figure 9, the LLZTO that was simply coated with a 100-nm-thick LiF layer *via* a thermal evaporator exhibited a much higher resistance than that of the uncoated LLZTO; thus, the overpotential was exceedingly large even at a low current density of  $0.1 \text{ mA cm}^{-2}$  unlike the case of  $\text{SnF}_2$ -treated LLZTO. Although further study is needed to elucidate the difference, we suspect that the presence of the Li-Sn alloy nanoparticles dispersed in the LiF matrix, as depicted in Figure 5g, could contribute to lowering the overpotential by promoting the lithium-ion transport in the medium.

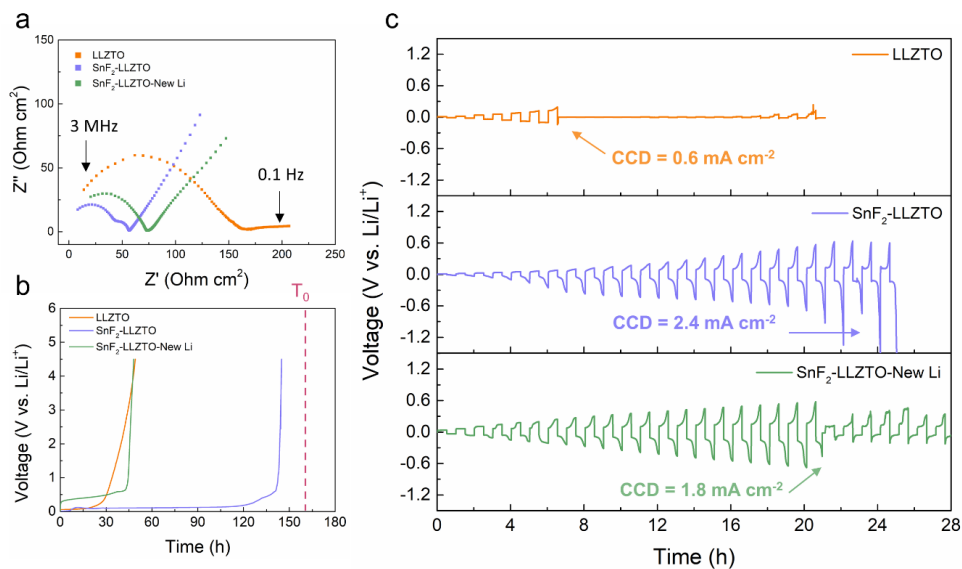


**Figure 6. Electrochemical stability of SnF<sub>2</sub>-modified LLZTO. a.** EIS spectra of Li symmetric cells at room temperature **b.** Potential profile during stripping at 0.2 mA cm<sup>-2</sup>. **c.** Critical current density measurement of Li symmetric cell at room temperature.

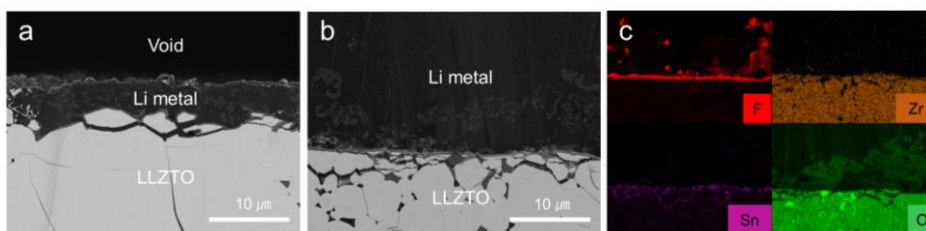


**Figure 7. Cross-sectional morphology.** **a.** Cross-sectional SEM image of  $\text{SnF}_2$ -treated LLZTO with Li metal removed. **b.** Cross-sectional SEM image of  $\text{SnF}_2$ -LLZTO with new Li attached without micro-sized Li–Sn alloy. **c.** Corresponding EDS mapping of F, Zr, Sn, and O elements from (b).



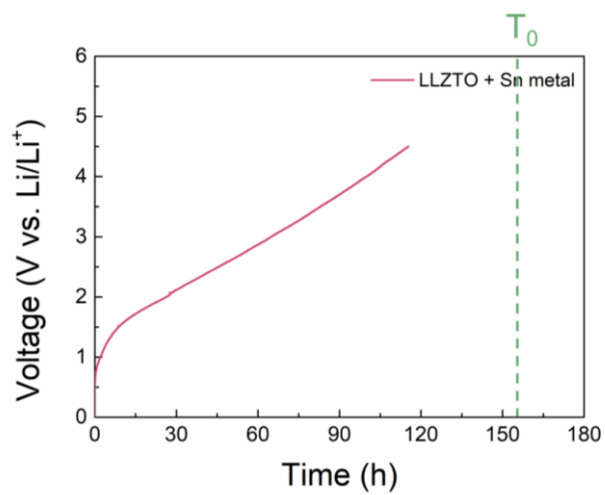


**Figure 8. Delithiation/stripping experiment.** Voltage–time curve of Li/LLZTO–Sn metal powder/Li symmetric cell at  $0.2 \text{ mA cm}^{-2}$ .

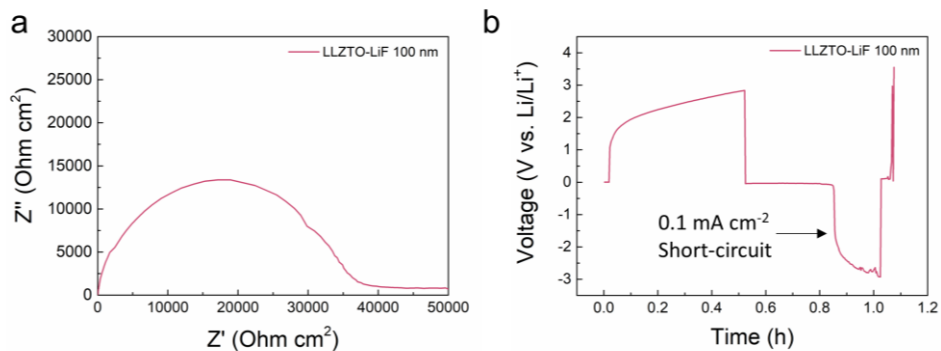


**Figure 9. Electrochemical characterization of LLZTO with 100 nm of LiF deposited.** **a.** Nyquist plot of Li/LLZTO–LiF/Li symmetric cell at room temperature. **b.** Critical current density measurement of Li/LLZTO–LiF/Li cell.

### 3.3 Electrochemical properties benefiting from artificial layer.

Figure 10a–b compare the long-term cycle stability of the lithium symmetric cells employing the SnF<sub>2</sub>-treated LLZTO and the uncoated LLZTO, respectively, at a current density of 0.5 mA cm<sup>-2</sup> at room temperature. The galvanostatic profile of the uncoated LLZTO indicates an initial overpotential of ~100 mV, which gradually increased with cycling. In addition, the short-circuit was observed in less than 20 hours, which is consistent with the previous results at the same current density.<sup>[48]</sup> In contrast, the SnF<sub>2</sub>-treated LLZTO cells could steadily maintain the stripping and deposition cycles for more than 1000 hours displaying an overpotential of approximately 80 mV without a significant increase with cycling. To scrutinize the stability of the interlayer after cycling, we disassembled the cells before the short-circuits occurred (~15 hours of galvanostatic cycling at a current density of 0.5 mA cm<sup>-2</sup>) and comparatively examined the interfaces, as shown in Figure 10c–d. The cross-sectional SEM images of the uncoated LLZTO and SnF<sub>2</sub>-treated LLZTO reveal that significant damage of the interface occurred for the uncoated LLZTO case, and pores and voids were extensively detected not only at the surface but also inside the solid electrolyte. These results indicate that the repeated stripping and deposition of lithium led to significant deterioration of the solid electrolyte structure near the interface, triggering the premature short-circuit of the uncoated LLZTO cells.<sup>[49, 50]</sup> In contrast, the SnF<sub>2</sub>-treated LLZTO maintained the initial interface structure without the apparent formation of defects, indicating that the interlayer contributed to the stability of the interface and the solid electrolyte during cycling. Inspired by the improved stability of the interface, we

additionally carried out the galvanostatic cycling tests at a higher current density of  $1.0 \text{ mA cm}^{-2}$  for the symmetric cell with the  $\text{SnF}_2$ -treated LLZTO. Figure 10e presents that it could also exhibit stable cycling performance for over 300 hours with a small increase in the overpotential from 160 to 310 mV. This result confirms that the multi-layer coating performed using a simple process could remarkably enhance the stability and compatibility of the LLZTO in contact with the lithium-metal electrode.

To further verify the viability of our strategy, a full cell was fabricated employing a lithium-metal anode, the  $\text{SnF}_2$ -treated LLZTO electrolyte, and a commercial  $\text{LiFePO}_4$  (LFP) cathode. Note that a small amount of ionic liquid electrolyte (2 M LiFSI in Pyr13FSI) was dropped on the LFP cathode to exclude the issue of the wetting between the LFP powder cathode and LLZTO pellet. Figure 11a shows the galvanostatic cycle performance of the cell for 600 cycles at a current density of  $1.0 \text{ mA cm}^{-2}$  for the lithium electrode, which corresponds to  $\sim 2$  C for the cathode at room temperature. It shows that the Li/garnet/LFP cell using  $\text{SnF}_2$ -treated LLZTO could exhibit remarkable cycling stability with a capacity of  $110 \text{ mAh g}_{\text{cathode}}^{-1}$  and a coulombic efficiency of over 99% after 600 cycles. For the comparisons, we attempted to cycle the full cell employing the uncoated LLZTO electrolyte at the same current density of  $1.0 \text{ mA cm}^{-2}$ ; however, failed cycling of the cell was observed at room temperature. The short-circuit of the cell with uncoated LLZTO was observed only after the first cycle at  $1.0 \text{ mA cm}^{-2}$ , revealing that lithium metal propagated inside the solid electrolyte at the current density (Figure 12). Instead, we cycled both cells at a current density that was ten times lower, *e.g.*,  $0.1 \text{ mA cm}^{-2}$  (or  $\sim 0.2$  C for the LFP cathode), which is moderately low enough to avoid the short-circuit. Figure 11b shows that the assembled Li/ $\text{SnF}_2$ -

treated LLZTO/LFP cell maintained a high capacity of 140 mAh  $g_{\text{cathode}}^{-1}$  without a noticeable capacity loss after 100 cycles, whereas the cell with the uncoated LLZTO suffered from capacity fading to 79% of the initial value and eventually reached a short-circuit after 80 cycles. The rate performance of the Li/SnF<sub>2</sub>-treated LLZTO/LFP was evaluated with current densities ranging from 0.1 C to 2 C in Figure 11c. The discharge capacities of the full cell were 144, 140, 132, 123, and 110 mAh  $g_{\text{cathode}}^{-1}$  at current densities of 0.05, 0.1, 0.25, 0.5, and 1.0 mA cm<sup>-2</sup>, respectively. As we restored the current rate to 0.2 C after 25 cycles of the rate test, the full cell recovered the initial discharge capacity of 144 mAh  $g_{\text{cathode}}^{-1}$ . Figure 11d shows that the typical discharge profile of the LFP cathode could be maintained in the Li/SnF<sub>2</sub>-treated LLZTO/LFP cell without a significant change. Additionally, we assembled a full cell employing a commercial LiNi<sub>1/3</sub>Co<sub>1/3</sub>Mn<sub>1/3</sub>O<sub>2</sub> cathode and performed similar electrochemical tests on the SnF<sub>2</sub>-treated LLZTO electrolyte. Figure 13 manifests that the SnF<sub>2</sub>-treated LLZTO also successfully served as a stable solid electrolyte for the LiNi<sub>1/3</sub>Co<sub>1/3</sub>Mn<sub>1/3</sub>O<sub>2</sub> cathode, delivering a capacity of approximately 130 mAh  $g_{\text{cathode}}^{-1}$  at a current density of 0.5 mA cm<sup>-2</sup> (~1 C) in the voltage range of 2.8–4.3 V for over 100 cycles. This finding indicates the general applicability of our multilayer strategy for various cathode materials for lithium batteries. In Figure 11e, the performance standings of our SnF<sub>2</sub>-treated LLZTO electrolyte are presented in comparison with representative previous reports on garnet-type solid electrolytes. [23, 25, 44, 45, 48, 51-54] The plot clearly shows that it has been challenging to achieve both high-rate capability and long durability from garnet-type solid electrolytes as indicated by the dotted line in the figure. The cycling performance with long-term stability (over 600 cycles) at a high rate (1.0 mA cm<sup>-2</sup>) in this work is unrivalled by that in previous research, supporting the

efficacy of the multilayer approach.

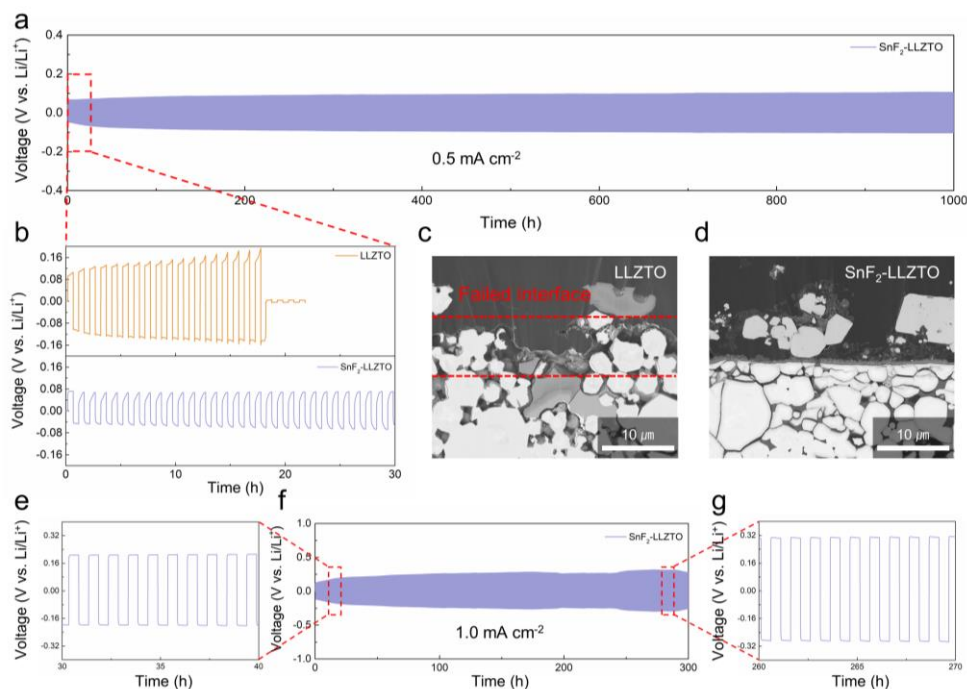


**Figure 10. Electrochemical performance of Li symmetric cells and SEM images of cycled LLZTO.** **a.** Long-term performance of Li/SnF<sub>2</sub>-treated LLZTO/Li symmetric cell with a current density of 0.5 mA cm<sup>-2</sup> at room temperature. **b.** Comparison of galvanostatic cycling for symmetric cells of uncoated LLZTO and SnF<sub>2</sub>-treated LLZTO at 0.5 mA cm<sup>-2</sup>. Cross-sectional SEM image of **c.** uncoated LLZTO interface and **d.** SnF<sub>2</sub>-treated LLZTO interface after cycling. **e–g.** Charge/discharge curves of Li/SnF<sub>2</sub>-treated LLZTO/Li cell at 1.0 mA cm<sup>-2</sup> at room temperature.

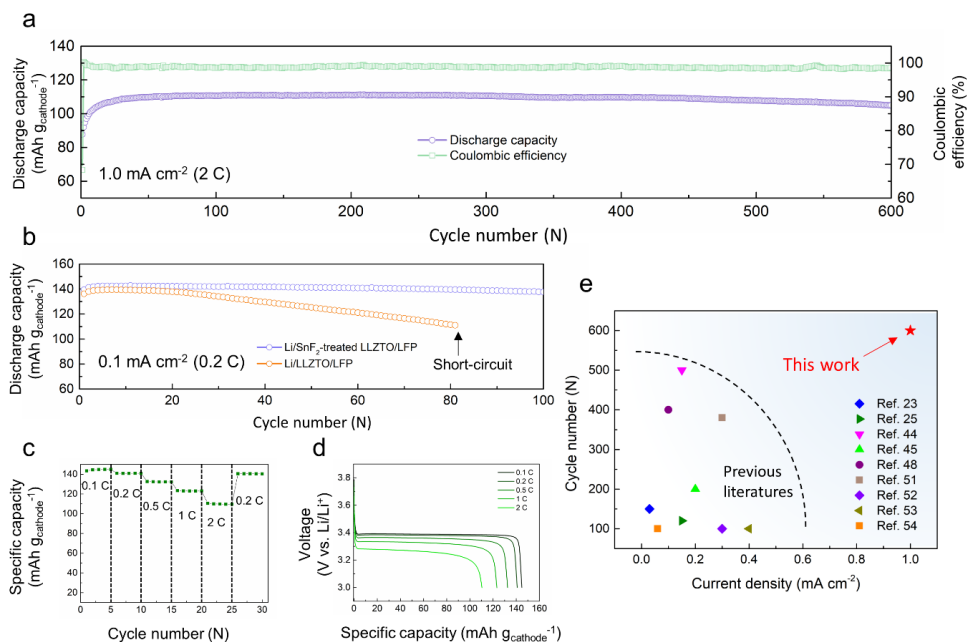


**Figure 11. Cycling performance of hybrid solid-state full cell.** **a.** Long-term performance of Li/SnF<sub>2</sub>-treated LLZTO/LiFePO<sub>4</sub> hybrid full cell with a current density of 1.0 mA cm<sup>-2</sup> at room temperature. **b.** Comparison of cyclability of hybrid cells of uncoated LLZTO and SnF<sub>2</sub>-treated LLZTO at 0.1 mA cm<sup>-2</sup>. **c.** Rate capability of SnF<sub>2</sub>-treated LLZTO full cell at different current densities. **d.** Voltage profile of Li/SnF<sub>2</sub>-treated LLZTO/LFP cell at different rates. **e.** Performance comparison of solid-state batteries with garnet-type solid electrolyte.



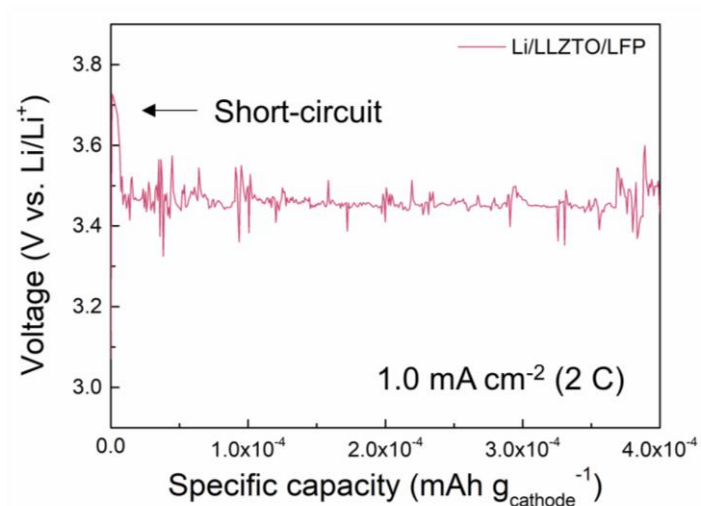


**Figure 12. Voltage profile of pristine LLZTO full cell.** 1<sup>st</sup> charge curve of Li/uncoated LLZTO/LFP hybrid full cell at 1.0 mA cm<sup>-2</sup> at room temperature.

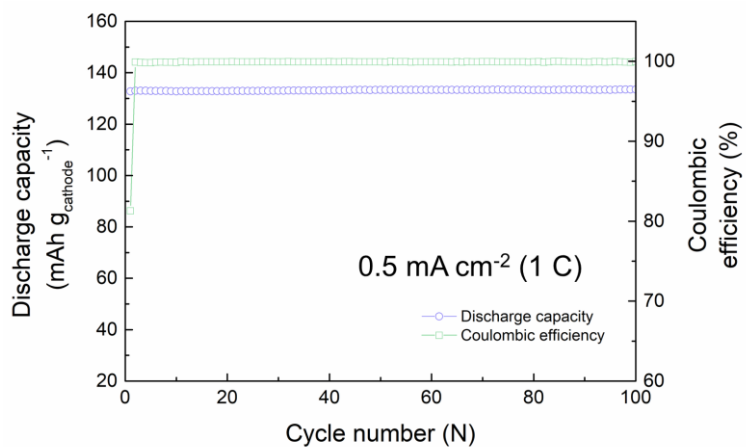


**Figure 13. Electrochemical characterization of hybrid solid-state full cell.**

Cycling performance of Li/SnF<sub>2</sub>-treated LLZTO/NCM111 hybrid cell at 0.5 mA cm<sup>-2</sup> at room temperature.

## Chapter 4. Conclusion

We have proposed a facile interface strategy exploiting the chemical conversion reaction between  $\text{SnF}_2$  and lithium metal to address the short-circuit issue caused by the lithium dendrite formation and propagation in garnet-type solid electrolytes. It was verified that a conformal LiF thin layer including Li–Sn alloys could be effectively formed on the surface of the solid electrolyte to reinforce the adhesion to lithium metal, leading to a lower interfacial resistance and preventing short-circuits even at a high current density of  $2.4 \text{ mA cm}^{-2}$  at room temperature. The Li–Sn alloy present in the lithium electrode enhanced the kinetics of lithium diffusion at the interface, suppressing the formation of voids and pores during the continuous cycling. Benefiting from this artificial interlayer, the lithium symmetric cell could achieve an outstanding cycle stability of over 1000 hours at  $0.5 \text{ mA cm}^{-2}$  and 300 hours at  $1.0 \text{ mA cm}^{-2}$ . These properties were further confirmed for full solid-state batteries of both LFP and  $\text{LiNi}_{1/3}\text{Co}_{1/3}\text{Mn}_{1/3}\text{O}_2$  cathodes, which exhibited stable capacity retention and high coulombic efficiency over 600 cycles. We believe that our strategy is widely applicable to other solid electrolytes due to its facile and simple low-temperature process. Considering the variety of conversion-based metal fluorides, further exploration is expected to identify the optimal solutions for garnet-type solid electrolytes in the future, which would expedite the development of all-solid-state batteries.

## Reference

- [1] W. Xu, J. Wang, F. Ding, X. Chen, E. Nasybulin, Y. Zhang, J.-G. Zhang, *Energy Environ. Sci.* **2014**, 7, 513.
- [2] Y. Guo, H. Li, T. Zhai, *Adv. Mater.* **2017**, 29, 1700007.
- [3] K. J. Harry, D. T. Hallinan, D. Y. Parkinson, A. A. MacDowell, N. P. Balsara, *Nat. Mater.* **2014**, 13, 69.
- [4] D. P. Finegan, M. Scheel, J. B. Robinson, B. Tjaden, I. Hunt, T. J. Mason, J. Millichamp, M. Di Michiel, G. J. Offer, G. Hinds, *Nat. Commun.* **2015**, 6, 1.
- [5] K. Oh, D. Chang, B. Lee, D.-H. Kim, G. Yoon, I. Park, B. Kim, K. Kang, *Chem. Mater.* **2018**, 30, 4995.
- [6] K. Yoon, J.-J. Kim, W. M. Seong, M. H. Lee, K. Kang, *Sci. Rep.* **2018**, 8, 1.
- [7] M. Balaish, J. C. Gonzalez-Rosillo, K. J. Kim, Y. Zhu, Z. D. Hood, J. L. Rupp, *Nat. Energy* **2021**, 1.
- [8] D. Chang, K. Oh, S. J. Kim, K. Kang, *Chem. Mater.* **2018**, 30, 8764.
- [9] A. Manthiram, X. Yu, S. Wang, *Nat. Rev. Mater.* **2017**, 2, 1.
- [10] N. Zhao, W. Khokhar, Z. Bi, C. Shi, X. Guo, L.-Z. Fan, C.-W. Nan, *Joule* **2019**, 3, 1.
- [11] J. Janek, W. G. Zeier, *Nat. Energy* **2016**, 1, 16141.
- [12] V. Thangadurai, S. Narayanan, D. Pinzar, *Chem. Soc. Rev.* **2014**, 43, 4714.
- [13] T. Thompson, S. Yu, L. Williams, R. D. Schmidt, R. Garcia-Mendez, J. Wolfenstine, J. L. Allen, E. Kioupakis, D. J. Siegel, J. Sakamoto, *ACS Energy Lett.* **2017**, 2, 462.

- [14] A. Gupta, R. Murugan, M. P. Paranthaman, Z. Bi, C. A. Bridges, M. Nakanishi, A. P. Sokolov, K. S. Han, E. Hagaman, H. Xie, *J. Power Sources* **2012**, 209, 184.
- [15] W. Xia, B. Xu, H. Duan, Y. Guo, H. Kang, H. Li, H. Liu, *ACS Appl. Mater. Interfaces* **2016**, 8, 5335.
- [16] C. Ma, Y. Cheng, K. Yin, J. Luo, A. Sharafi, J. Sakamoto, J. Li, K. L. More, N. J. Dudley, M. Chi, *Nano Lett.* **2016**, 16, 7030.
- [17] E. Kazyak, R. Garcia-Mendez, W. S. LePage, A. Sharafi, A. L. Davis, A. J. Sanchez, K.-H. Chen, C. Haslam, J. Sakamoto, N. P. Dasgupta, *Matter* **2020**, 2, 1025.
- [18] T. Krauskopf, R. Dippel, H. Hartmann, K. Peppler, B. Mogwitz, F. H. Richter, W. G. Zeier, J. Janek, *Joule* **2019**, 3, 2030.
- [19] F. Aguesse, W. Manalastas, L. Buannic, J. M. Lopez del Amo, G. Singh, A. Llordés, J. Kilner, *ACS Appl. Mater. Interfaces* **2017**, 9, 3808.
- [20] E. J. Cheng, A. Sharafi, J. Sakamoto, *Electrochim. Acta* **2017**, 223, 85.
- [21] T. Famprikis, P. Canepa, J. A. Dawson, M. S. Islam, C. Masquelier, *Nat. Mater.* **2019**, 18, 1278.
- [22] R. G. Fedorov, S. Maletti, C. Heubner, A. Michaelis, Y. Ein-Eli, *Adv. Energy Mater.* **2021**, 11, 200648.
- [23] H. Huo, Y. Chen, N. Zhao, X. Lin, J. Luo, X. Yang, Y. Liu, X. Guo, X. Sun, *Nano Energy* **2019**, 61, 119.
- [24] X. Han, Y. Gong, K. K. Fu, X. He, G. T. Hitz, J. Dai, A. Pearse, B. Liu, H. Wang, G. Rubloff, *Nat. Mater.* **2017**, 16, 572.
- [25] Y. Ruan, Y. Lu, X. Huang, J. Su, C. Sun, J. Jin, Z. Wen, *J. Mater. Chem. A* **2019**, 7, 14565.

- [26] H. Duan, W. P. Chen, M. Fan, W. P. Wang, L. Yu, S. J. Tan, X. Chen, Q. Zhang, S. Xin, L. J. Wan, *Angew. Chem., Int. Ed.* **2020**, *59*, 12069.
- [27] M. Wang, J. Sakamoto, *J. Power Sources* **2018**, *377*, 7.
- [28] L. Yang, Z. Lu, Y. Qin, C. Wu, C. Fu, Y. Gao, J. Liu, L. Jiang, Z. Du, Z. Xie, *J. Mater. Chem. A* **2021**.
- [29] J. Kasemchainan, S. Zekoll, D. S. Jolly, Z. Ning, G. O. Hartley, J. Marrow, P. G. Bruce, *Nat. Mater.* **2019**, *18*, 1105.
- [30] K. B. Hatzell, X. C. Chen, C. L. Cobb, N. P. Dasgupta, M. B. Dixit, L. E. Marbella, M. T. McDowell, P. P. Mukherjee, A. Verma, V. Viswanathan, A. S. Westover and W. G. Zeier, *ACS Energy Lett.* **2020**, *5*, 922.
- [31] T. Krauskopf, B. Mogwitz, C. Rosenbach, W. G. Zeier, J. Janek, *Adv. Energy Mater.* **2019**, *9*, 1902568.
- [32] S. Jin, Y. Ye, Y. Niu, Y. Xu, H. Jin, J. Wang, Z. Sun, A. Cao, X. Wu, Y. Luo, *J. Am. Chem. Soc.* **2020**, *142*, 8818.
- [33] S. Kim, C. Jung, H. Kim, K. E. Thomas-Alyea, G. Yoon, B. Kim, M. E. Badding, Z. Song, J. Chang, J. Kim, *Adv. Energy Mater.* **2020**, *10*, 1903993.
- [34] F. Han, A. S. Westover, J. Yue, X. Fan, F. Wang, M. Chi, D. N. Leonard, N. J. Dudney, H. Wang, C. Wang, *Nat. Energy* **2019**, *4*, 187.
- [35] Y. Song, L. Yang, W. Zhao, Z. Wang, Y. Zhao, Z. Wang, Q. Zhao, H. Liu, F. Pan, *Adv. Energy Mater.* **2019**, *9*, 1900671.
- [36] H. Buschmann, S. Berendts, B. Mogwitz, J. Janek, *J. Power Sources* **2012**, *206*, 236.
- [37] W. Xia, B. Xu, H. Duan, X. Tang, Y. Guo, H. Kang, H. Li, H. Liu, *J. Am. Ceram. Soc.* **2017**, *100*, 2832.
- [38] R. Pathak, K. Chen, A. Gurung, K. M. Reza, B. Bahrami, J. Pokharel, A.

- Baniya, W. He, F. Wu, Y. Zhou, *Nat. Commun.* **2020**, *11*, 1.
- [39] Z. Tu, S. Choudhury, M. J. Zachman, S. Wei, K. Zhang, L. F. Kourkoutis, L. A. Archer, *Nat. Energy* **2018**, *3*, 310.
- [40] J. York-Winegar, T. Harper, C. Brennan, J. Oelgoetz, A. Kovalskiy, *Phys. Procedia* **2013**, *44*, 159.
- [41] J. Fu, P. Yu, N. Zhang, G. Ren, S. Zheng, W. Huang, X. Long, H. Li, X. Liu, *Energy Environ. Sci.* **2019**, *12*, 1404.
- [42] C.-L. Tsai, V. Roddatis, C. V. Chandran, Q. Ma, S. Uhlenbruck, M. Bram, P. Heitjans, O. Guillon, *ACS Appl. Mater. Interfaces* **2016**, *8*, 10617.
- [43] D. C. Sinclair, *Bol. Soc. Esp. Ceram. Vidrio* **1995**, *34*, 55.
- [44] J. Meng, Y. Zhang, X. Zhou, M. Lei, C. Li, *Nat. Commun.* **2020**, *11*, 3716.
- [45] Y. Ruan, Y. Lu, Y. Li, C. Zheng, J. Su, J. Jin, T. Xiu, Z. Song, M. E. Badding, Z. Wen, *Adv. Funct. Mater.* **2020**, 2007815.
- [46] L. Chen, K.-S. Chen, X. Chen, G. Ramirez, Z. Huang, N. R. Geise, H.-G. Steinrück, B. L. Fisher, R. Shahbazian-Yassar, M. F. Toney, *ACS Appl. Mater. Interfaces* **2018**, *10*, 26972.
- [47] L. Fan, H. L. Zhuang, L. Gao, Y. Lu, L. A. Archer, *J. Mater. Chem. A* **2017**, *5*, 3483.
- [48] T. Deng, X. Ji, Y. Zhao, L. Cao, S. Li, S. Hwang, C. Luo, P. Wang, H. Jia, X. Fan, *Adv. Mater.* **2020**, *32*, 2000030.
- [49] S. Hao, J. J. Bailey, F. Iacoviello, J. Bu, P. S. Grant, D. J. Brett, P. R. Shearing, *Adv. Funct. Mater.* **2021**, *31*, 2007564.
- [50] B. Wu, S. Wang, J. Lochala, D. Desrochers, B. Liu, W. Zhang, J. Yang, J. Xiao, *Energy Environ. Sci.* **2018**, *11*, 1803.
- [51] Y. Zhong, Y. Xie, S. Hwang, Q. Wang, J. J. Cha, D. Su, H. Wang, *Angew.*

*Chem., Int. Ed.* **2020**, *59*, 14003.

[52] X. Zhang, Q. Xiang, S. Tang, A. Wang, X. Liu, J. Luo, *Nano Lett.* **2020**, *20*, 2871.

[53] Y. Lu, X. Huang, Y. Ruan, Q. Wang, R. Kun, J. Yang, Z. Wen, *J. Mater. Chem. A* **2018**, *6*, 18853.

[54] J. Lou, G. Wang, Y. Xia, C. Liang, H. Huang, Y. Gan, X. Tao, J. Zhang, W. Zhang, *J. Power Sources* **2020**, *448*, 227440.



## Abstract in Korean

차세대 교통수단으로 전기자동차에 대한 관심이 급증함에 따라, 고 에너지 밀도를 가지는 안전한 리튬이온 이차전지에 대한 요구가 지속적으로 발생하고 있다. 그에 따라 최근 리튬 메탈을 음극으로 사용하는 전고체 전지가 각광을 받고 있지만, 불균일한 리튬 성장으로 인한 단락 현상이 주요한 문제점으로 지적되고 있다. 가넷 타입의 산화물 고체 전해질에서 불균일한 리튬 성장의 원인으로 전해질과 전극 사이 계면의 결함, 고체 전해질의 높은 전자전도도, 충 방전 과정에서 계면의 붕괴 등이 있으며, 이를 해결하기 위해 계면을 안정적으로 유지시켜 줄 수 있는 중간층을 도입하는 연구들이 많이 진행되어 왔다. 하지만 높은 전류밀도에서 단락 현상이 여전히 관찰되고 있으며, 기존의 연구들은 공정 도입의 어려움 등으로 인해 상용화에 어려움을 겪고 있다. 본 연구에서, 우리는 플루오린화 주석과 리튬 메탈의 간단한 화학반응을 통해 플루오린화 리튬 및 리튬-주석 합금으로 구성된 다기능 계면을 리튬 메탈과 고체 전해질 사이에 형성시켜 전기화학 특성을 개선하고자 한다. 플루오린화 리튬은 고체 전해질 표면에서 수백 나노의 두께를 가지는 얇은 막으로 형성되어, 초기 계면 저항을 감소시키고 높은 임계전류밀도 값을 가지도록 도움을 준다. 한편, 리튬-주석 합금은 리튬 메탈 내부에 수 마이크로 크기로 존재하며, 리튬 이온의 동특성을 개선하여 지속적인 리튬 탈리 과정에서 계면의 안정성을 높이는데 기여를 한다. 플루오린화 리튬을 통해 계면을 개선한 고체 전해질의 리튬 대칭 셀 시스템에서 1000시간 이상

의 안정적인 사이클 특성을 보였으며, 극단적인 조건인  $1.0 \text{ mA cm}^{-2}$ 에서조차 600 사이클 후에도 단락 없이 평탄한 전압을 보여주었다. 또한  $\text{LiFePO}_4$  및 NCM111 양극을 사용한 풀 셀에서도 600 사이클 후에도 높은 용량 유지율을 보여줌으로써 가넷 타입의 산화물 고체 전해질의 활용에 주요한 전략으로 활용될 수 있음을 입증하였다.

**주요어:** 리튬 이온 이차전지, 가넷 타입 고체 전해질, 플루오린화 주석, 불균일한 리튬 성장, 계면,

**학번:** 2019-28030